Earth and Planetary Science Letters 287 (2009) 529–539

Contents lists available at ScienceDirect

Earth and Planetary Science Letters

journal homepage: www.elsevier.com/locate/epsl

Geomagnetic intensity spike recorded in high resolution slag deposit in Southern Jordan

Erez Ben-Yosef [a,*], Lisa Tauxe [b], Thomas E. Levy [a], Ron Shaar [c], Hagai Ron [c], Mohammad Najjar [d]

[a] Department of Anthropology, University of California, San Diego, La Jolla, CA 92093, United States
[b] Scripps Institution of Oceanography, University of California, San Diego, La Jolla, CA 92093, United States
[c] Institute of Earth Sciences, The Hebrew University of Jerusalem, Jerusalem, 91904, Israel
[d] Friends of Archaeology and Heritage Society, P.O. Box 2440, Amman 11181, Jordan

ARTICLE INFO

Article history:
Received 9 June 2009
Received in revised form 29 August 2009
Accepted 1 September 2009
Available online 26 September 2009

Editor: P. DeMenocal

Keywords:
archaeomagnetism
paleomagnetism
secular variations
Iron Age
copper slag
Faynan
archaeometallurgy
radiocarbon

ABSTRACT

In paleomagnetism, periods of high field intensity have been largely ignored in favor of the more spectacular directional changes associated with low field intensity periods of excursions and reversals. Hence, questions such as how strong the field can get and how fast changes occur are still open. In this paper we report on data obtained from an archaeometallurgical excavation in the Middle East, designed specifically for archaeomagnetic sampling. We measured 342 specimens from 72 samples collected from a 6.1 m mound of well stratified copper production debris at the early Iron Age (12th–9th centuries BCE) site of Khirbat en-Nahas in Southern Jordan. Seventeen samples spanning 200 yr yielded excellent archaeointensity results that demonstrate rapid changes in field intensity in a period of overall high field values. The results display a remarkable spike in field strength, with sample mean values of over 120 μT (compared to the current field strength of 44 μT). A suite of 13 radiocarbon dates intimately associated with our samples, tight control of sample location and relative stratigraphy provide tight constraints on the rate and magnitude of changes in archaeomagnetic field intensities.

1. Introduction

Study of the ancient geomagnetic field has widespread implications for a variety of disciplines including physics of the Earth's interior (e.g., Christensen and Wicht, 2007), tectonics (e.g., Torsvik et al., 2008), the early history of the Earth (e.g., Tarduno et al., 2006), biostratigraphy (e.g., Opdyke and Channell, 1996), and archaeomagnetic dating (e.g., Lanos, 2003). Our understanding of the geomagnetic field is based on data obtained from historical measurements (e.g., Jackson et al., 2000; Jackson, 2003), archaeological and geological samples (e.g., Korte and Constable, 2005) and numerical simulations (e.g., Glatzmaier and Roberts, 1996). However, despite centuries of research, we still lack sufficient information regarding such fundamental properties of its behavior as the maximum field strength or its maximum rate of change. Therefore, reliable data from tightly controlled chronostratigraphic contexts are still essential for enhancing our knowledge.

Encouraged by the results of Ben-Yosef et al. (2008a,b) we designed a high resolution sampling strategy for archaeointensity investigation and, aiming at a probable period of a high intensity field around the 10th century BCE (Genevey et al., 2003; Pressling et al., 2006; Ben-Yosef et al., 2008a), applied it as part of the excavation project of the University of California, San Diego and the Department of Antiquities of Jordan, reported by Levy et al. (2008). The excavation penetrated one of the numerous 'slag mounds' at the site of Khirbat en-Nahas (latitude 30.681°N, longitude 35.437°E, Fig. 1), one of the largest ancient copper production centers in the Southern Levant. Three months of careful excavation into approximately 6.1 m of archaeological accumulation exposed a complex sequence of fine industrial debris layers and resulted in a large inventory of samples from a well controlled context. We recorded the x, y and z coordinates of each sample using a 'total station' (precision of less than 5 cm) and included detailed descriptions of their setting in relation to the general division of excavation units (square, strata, loci and baskets). As the site is characterized mostly by pyrotechnological refuse and is located in an arid region where organic material is frequently preserved, it was relatively easy to obtain suitable charcoal samples closely associated with samples for archaeointensity experiments. Radiocarbon measurements of these samples are the basis for the age constraints of the archaeointensity data, as explained below.

2. Archaeointensity experiments

Samples for archaeointensity experiments include copper slag fragments, pieces of smelting furnaces (burned clay) and tuyères (clay

* Corresponding author.
E-mail address: ebenyose@ucsd.edu (E. Ben-Yosef).

0012-821X/$ – see front matter © 2009 Elsevier B.V. All rights reserved.
doi:10.1016/j.epsl.2009.09.001

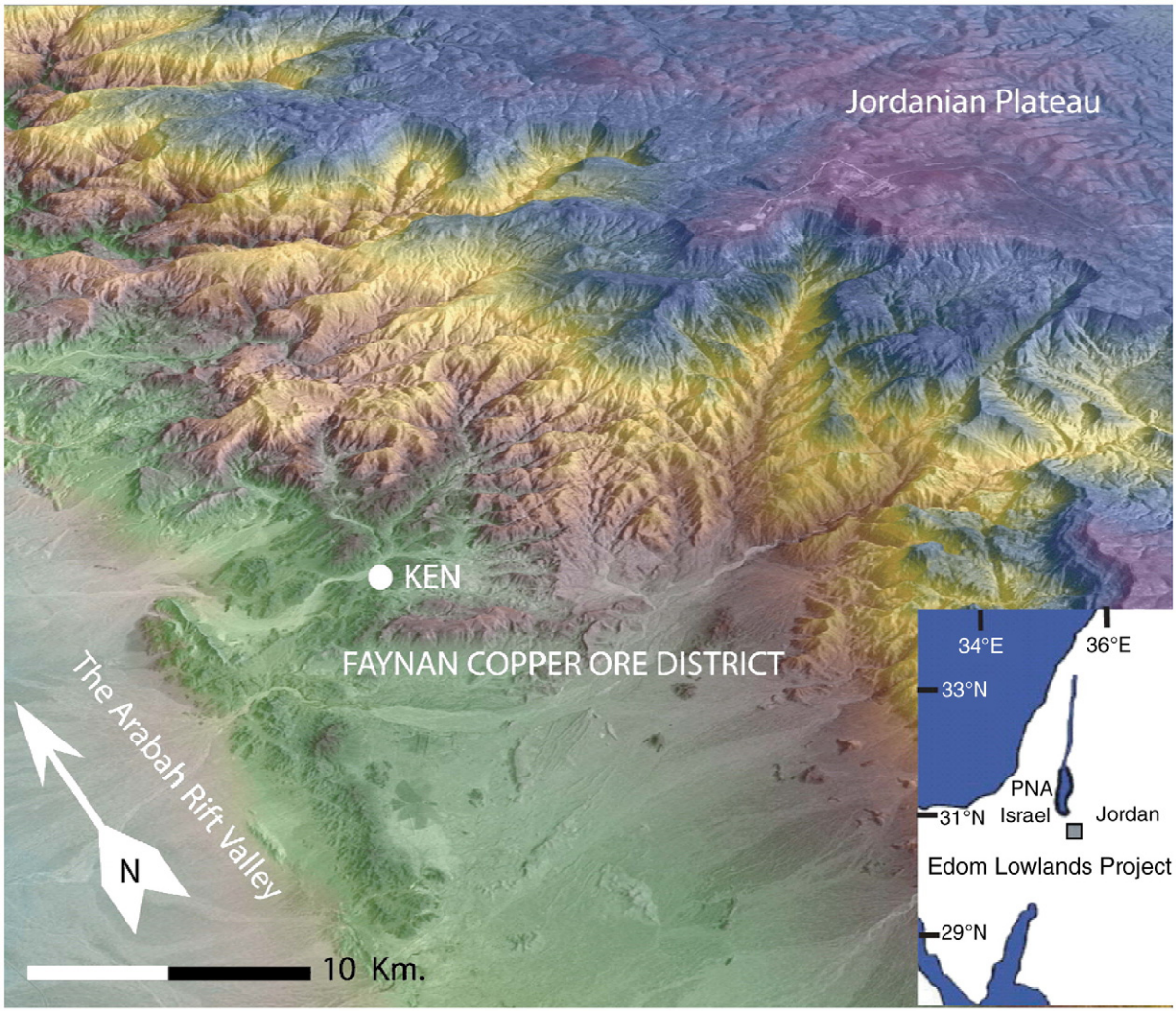

Fig. 1. Faynan Copper Ore District in Southern Jordan, with the archaeological site of Khirbat en-Nahas (KEN), the largest Iron Age copper production center in the Southern Levant. False color 3D satellite image courtesy of Richard Cleave, ROHR, Nicosia, Cyprus. (For interpretation of the references to color in this figure legend, the reader is referred to the web version of this article.)

nozzles of bellow pipes), as well as a few pottery sherds. Ben-Yosef et al. (2008a) demonstrated the reliability of copper slag and associated clay material as archaeointensity recorders and summarized the advantages of its exploitation for reconstructing geomagnetic field intensities for the period of the last seven millennia, starting with the introduction of metallurgy in human history. Their conclusions are based on testing slag material under controlled conditions (known field intensities were recovered from re-melted slag materials), and on results from a large collection of slag samples that were compared to burned clay from the same contexts and to other datasets from the Levant. All of the samples in the current study were divided into 4–12 specimens that were subjected to the Thellier–Thellier based IZZI paleointensity protocol (Tauxe and Staudigel, 2004), including 'pTRM checks' and 'pTRM tail checks'. Representative results from slag material are shown in Fig. 2 and examples of pottery, tuyère and furnace fragments are shown in Fig. 3. Heating steps followed by cooling either in zero field or a controlled lab field (30, 50 or 70 μT) enables graphic depiction (an 'Arai plot' — see Figs. 2a–c and 3a–c for examples) of the remaining original magnetization (natural remanent magnetization, NRM) versus field acquired remanence for each temperature level (partial thermal remanent magnetization, pTRM gained). The absolute value of the slope relating the two, when multiplied by the laboratory field allows calculation of the ancient magnetic field. The pTRM checks and tail checks are also graphically illustrated for facilitating evaluation of specimen quality (shown as triangles and squares respectively in the plots shown in Figs. 2a–c and 3a–c).

To further illustrate the behavior of each specimen in the archaeointensity experiment we show the evolution of the directional results as equal area projections with vector end-point diagrams (see Figs. 2d–f and 3d–f for examples). In the equal area projections, we show the change in natural remanent directions as circles and squares and the directions of the pTRMs acquired in each in-field step as triangles. If the pTRMs are acquired in a direction deflected from the laboratory field direction (center of the diagram), then there is cause for worry about the anisotropy of the TRM. Here we use a new paleointensity statistic, γ, defined by Tauxe (2009), which is the angle between the applied field and the best-fit line through the pTRM data.

Many specimens, including nearly all of those with significantly deflected pTRMs, were treated to anisotropy of anhysteretic remanence (AARM) experiments (some deflected specimens were not subjected to this treatment because they broke during or prior to the AARM experiment). In addition, 57 specimens were also subjected to a TRM anisotropy experiment (ATRM). There was no significant difference between the ATRM and the AARM corrected results.

In addition to the standard paleointensity experiment, we tested representative specimens for non-linearity of TRM acquisition (Selkin et al., 2007) (see, e.g., S10265 in Fig. 2). After correction for non-linear TRM acquisition when applicable (B_{nlc} in Fig. 2), specimens were also

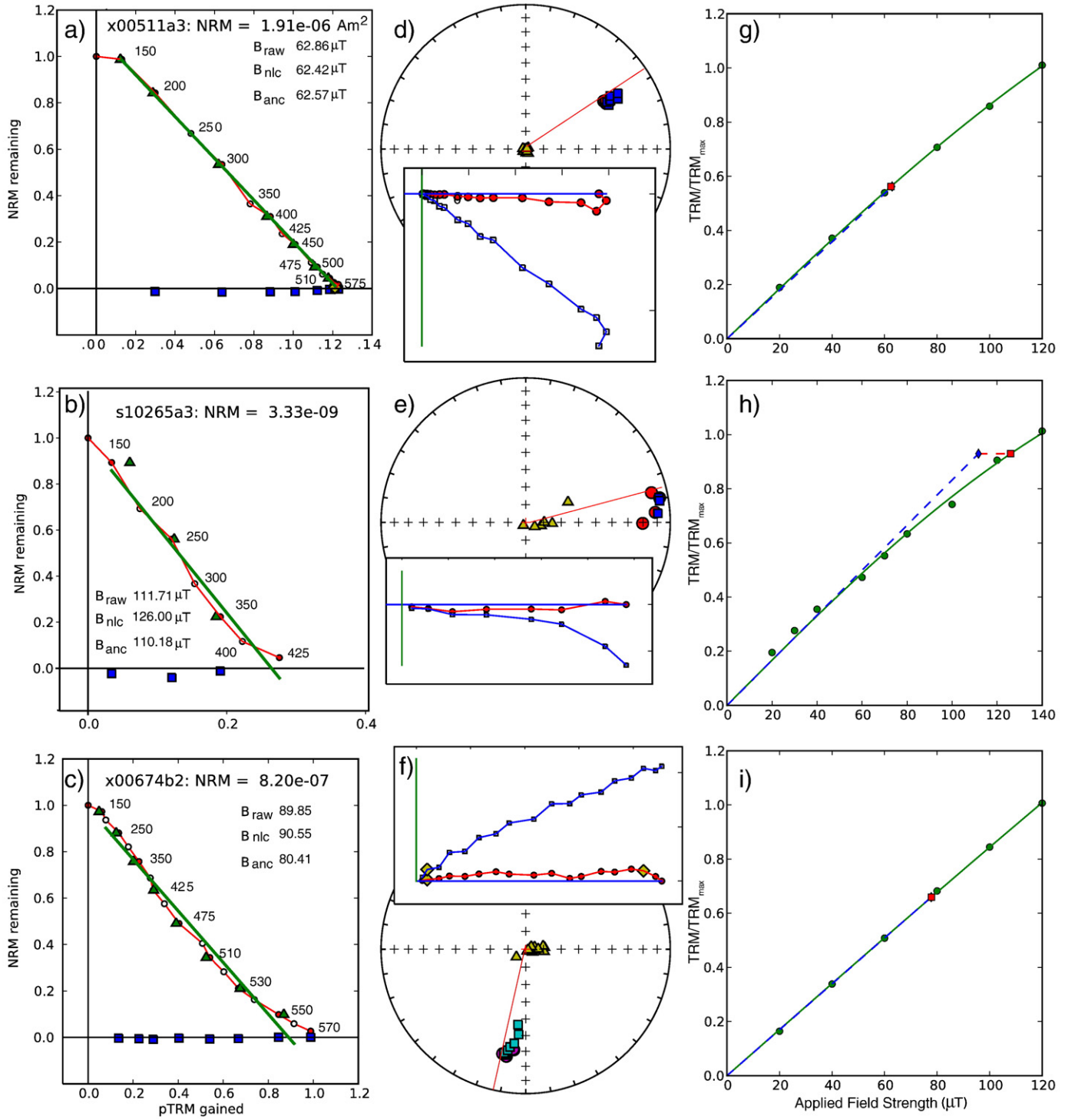

Fig. 2. Examples of results from the archaeointensity experiments, slag material: a–c) Arai plots are shown together with the calculated ancient field [B_{raw}, the slope of green line times laboratory field, B_{nlc}, corrected for non-linear TRM acquisition (see g–i), B_{anc} corrected for remanence anisotropy]. Open (closed) circles are the IZ (ZI) steps. Triangles (squares) are the pTRM (tail) check steps. NRM intensities are in Am^2. d–f) Directional results plotted as equal area projections with vector end-point diagrams shown as insets. The solid line from the center to the edge of the equal area projections is the direction of the NRM, which serves as the X axis direction in the vector end-point diagrams. The triangles in the equal area projections are upper hemisphere projections of the directions of the pTRM gained at in-field temperature step. The applied field was at the center of the diagram (in the up direction). Offset from the applied field direction implies significant anisotropy of remanence; requires anisotropy correction. Circles (squares) are ZI (IZ) steps and closed (open) symbols are lower (upper) hemisphere projections. g–i) TRM acquisition experiments. Specimens are given a total TRM by heating to 600 °C and cooled in varying applied fields (dots). The data are fit with the best-fit hyperbolic tangent (solid line). B_{raw} (diamond) is found using the linear acquisition assumption. The actual field required to produce the same TRM (square) is B_{nlt}. (For interpretation of the references to color in this figure legend, the reader is referred to the web version of this article.)

corrected for anisotropy of remanence, using anhysteretic remanence (AARM) as a proxy (B_{anc} in Fig. 2). Specimens of pyrotechnological artifacts of the ancient copper industry experienced relatively fast cooling (Ben-Yosef et al., 2008a), and do not require cooling rate corrections.

To interpret the paleointensity data, we depart from previous practice of Ben-Yosef et al. (2008a,b) which aimed at recovering a robust average field strength at each location. Here we are seeking the most precise paleointensity estimates for each individual horizon. There is no

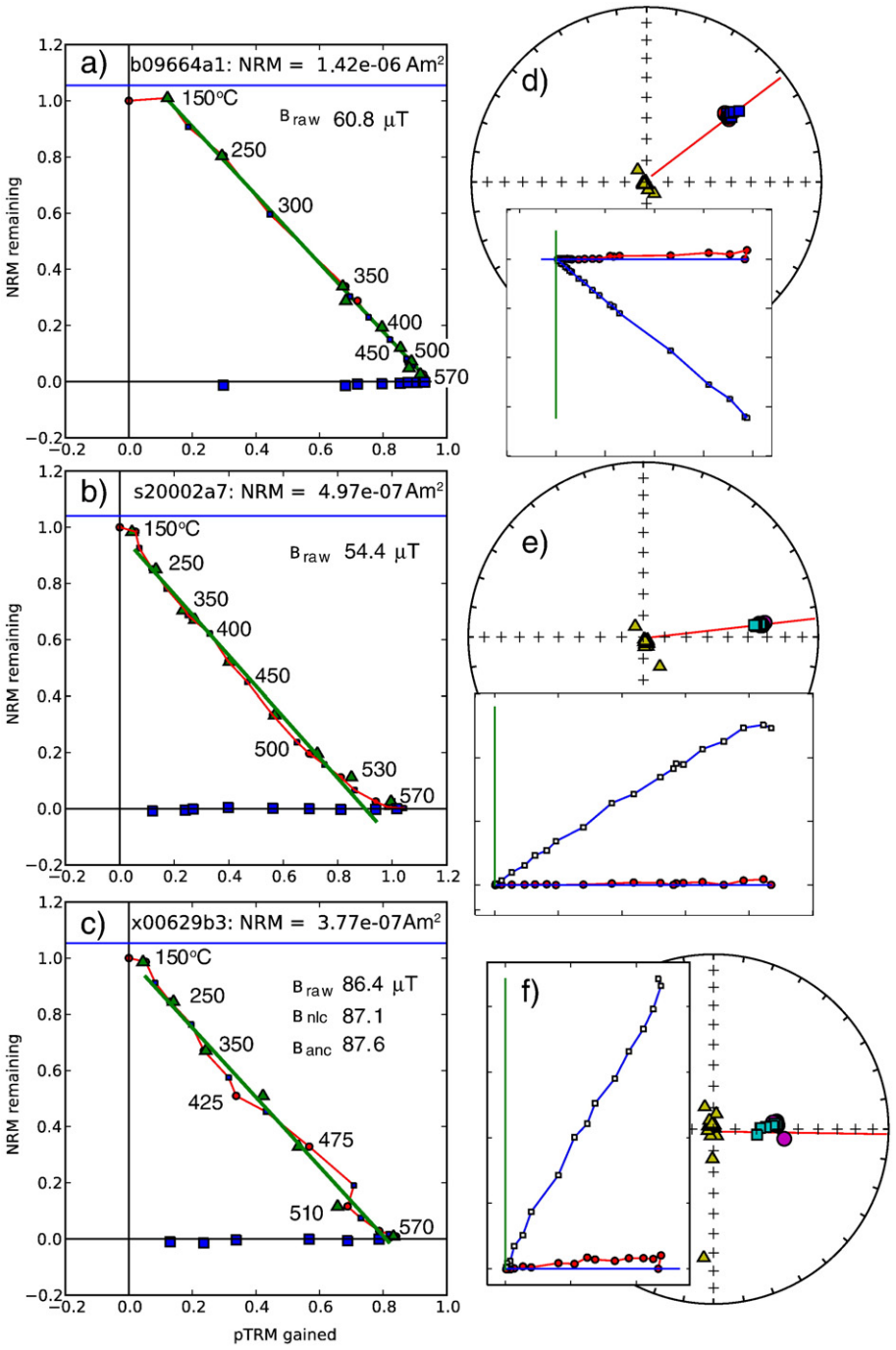

Fig. 3. Examples of results from the archaeointensity experiments, burned clay: a–c) Arai plots (see key in Fig. 2). d–f) Directional results plotted as equal area projections with vector end-point diagrams shown as insets (see key in Fig. 2). Specimen b09664a1 is a pot sherd, s20002a7 is a tuyère and x00629b3 is a furnace fragment.

consensus in the scholarly literature concerning paleointensity selection criteria and no set of cut-off values for the myriad ways of characterizing data quality guarantees that a given result is reliable. Most studies recognize that single component vector end-point diagrams and single slope Arai plots are desirable and exclude many uncertainties in the interpretation process. Therefore, we use only results that had a single component of remanence that decayed to the origin associated with a single slope in the Arai plot. To insure that each specimen had only one component, the included steps must comprise at least 70% of the NRM vector and the maximum treatment step included in the slope calculation was at most 10% of the original NRM. The requirement of a single component of remanence (both in direction and on the Arai plot) insures that partially re-heated samples will be excluded because slag, furnace material and tuyères that are moved during cooling, or re-heated by contact with subsequent smelting debris display complex directional behavior of the remanence. In addition, here we applied the criteria listed in Table 1 for selection of specimens. This includes the Difference RATio

Table 1
Summary of acceptance criteria.

DRATS	β	f_{vds}	MAD	DANG	σ%	N_{min}
20	0.1	0.7	10	10	20%	2

σ [σ%]: standard deviation cut-off for sample means [expressed as percentage of mean of specimens per sample], N_{min}: minimum of specimens per sample (for further explanations and references see Ben-Yosef et al. 2008a).

Table 2
A summary of all 'successful' specimens.

Specimen	T_{min}	T_{max}	f_{vds}	DRATS (%)	N	β	DANG	q	γ	B_{lab} (μT)	B_{raw} (μT)	B_{nlt} (μT)	B_{ani} (μT)
b09664a1	150	560	0.94	7.5	18	0.008	0.4	95	1.7	50	60.8		
b09664a2	150	560	0.953	6.7	18	0.008	0.2	95.8	2.4	50	61.5		
b09664a3	150	570	0.958	8.5	19	0.01	0.4	71.1	3.5	50	66.9		
b09664a4	150	560	0.921	8.6	18	0.009	0.2	80.9	1.6	50	64.5		
b09664a5	150	560	0.949	9.7	18	0.009	0.3	84.3	1.1	50	60.3		
e10462a3	100	400	0.734	5.9	7	0.03	0.6	11.8	3.9	30	53.1	54.1	54.9
e10462a4	150	350	0.868	2.6	5	0.046	2.7	9.7	3.2	70	60.1		59.7
e10462a6	150	350	0.706	1.3	5	0.032	4.6	10.5	4.9	70	57.5		56.4
e10466a1	150	450	0.817	0.2	7	0.085	2.9	8.3	8.6	30	81.9		
e10466a2	150	300	0.718	3.6	4	0.059	3.4	9.3	19.7	30	61.9		51.5
e10466a5	0	400	0.941	2.7	7	0.024	1.4	34.3	7.2	70	57.6		47.5
e10474a1	0	400	0.732	11	8	0.053	9.5	14.9	1	30	85.8		85.8
e10474a6	0	400	0.889	2	7	0.033	2.8	23.1	1.8	70	74.8		
e10482a1	100	350	0.903	5.3	6	0.015	0.9	44.6	4.1	30	66.1	67.7	68.7
e10482a2	100	350	0.903	2.7	6	0.041	0.4	17	3	30	64.0	65.0	62.7
e10482a5	0	400	0.925	5.8	7	0.031	3.1	25.6	3.1	70	69.5		67.1
e10482a6	0	350	0.95	3	6	0.031	3.8	25.1	1.8	70	69.1		70.9
e10482a7	0	350	0.969	0.2	6	0.013	1.4	59.8	2.9	70	69.6		66.7
s10259a2	100	400	0.812	12.1	7	0.056	6.7	12.4	6.8	30	115.5	130.1	143.6
s10259a6	150	350	0.766	18.5	5	0.065	3.2	8.1	3.2	70	79.0		79.6
s10259a8	150	350	0.748	12	5	0.097	6	5.4	9	70	84.3		84.0
s10259a9	150	400	0.787	16.9	6	0.074	6.5	7.6	1.2	70	63.5		
s10265a10	150	425	0.746	8	7	0.098	3.9	6.6	1.2	70	105.4		100.9
s10265a12	0	450	0.971	14.7	9	0.09	4	7.9	9.6	70	105.9		
s10265a2	100	400	0.779	2.8	7	0.022	3.1	32.7	9.7	30	92.5	99.3	100.2
s10265a3	100	400	0.845	8.4	7	0.074	3.4	10	5.6	30	111.7	126.0	124.3
s10265a9	0	425	0.931	8.3	8	0.047	4.6	16	5.2	70	121.0		119.7
s10267a5	150	300	0.872	3.1	4	0.055	0.8	8.9	1.5	50	60.4		
s10272a3	0	350	0.934	5.2	7	0.075	9.4	11.5	2.8	30	212.2		221.0
s10274a3	0	400	0.818	4.4	8	0.08	7.1	9.6	1.2	30	90.3		85.9
s10280a2	0	250	0.895	6.9	5	0.085	6	8.9	2.5	30	69.4		64.0
s20001a1	150	540	0.821	1.9	16	0.027	2.8	29.5	3.8	50	73.9		
s20001a3	150	540	0.871	2.1	16	0.031	2.1	27.5	1.9	50	76.4		
s20002a1	150	550	0.868	9.7	17	0.03	3.2	28.9	2.8	50	56.9		
s20002a2	150	500	0.86	8.1	12	0.042	0.7	18.9	1.4	50	63.0		
s20002a3	150	500	0.783	3.8	12	0.057	3	14.9	2.5	50	58.7		
s20002a4	150	560	0.87	1.1	18	0.022	2	38.9	5.6	50	73.6		
s20002a5	150	560	0.876	1.6	18	0.03	1.9	29.1	4.1	50	59.6		
s20002a6	150	560	0.855	4.7	18	0.033	1.7	26.2	1.9	50	68.2		
s20002a7	150	550	0.922	8.1	17	0.026	1.2	35.5	4	50	54.4		
s20002a8	150	540	0.858	4.8	16	0.026	2.1	30.5	2.8	50	56.9		
s20002a9	150	540	0.897	10.5	16	0.019	1.6	46.5	4	50	55.9		
s20003a4	0	540	0.834	9.8	17	0.026	7.4	35.5	3.9	50	64.8		
s20005a4	150	540	0.91	17.8	16	0.02	1.3	41.3	1.6	50	63.3		
s20007a1	150	570	0.782	2	19	0.034	1.2	19.1	3.8	50	76.2		
s20007a2	150	570	0.806	11.1	19	0.031	1.3	21.7	4.1	50	72.6		
s20007a3	150	570	0.784	0.5	19	0.034	1.7	19.1	4.6	50	72.5		
s20007a4	150	570	0.82	10.6	19	0.033	0.9	20.5	3.1	50	76.4		
s20007a5	150	570	0.775	0.2	19	0.034	0.4	18.9	4	50	89.8		
x00511a1	0	520	0.922	6.2	13	0.031	0.9	25	2.2	70	67.9	67.8	65.0
x00511a2	150	550	0.852	7.3	15	0.012	2.3	66.1	1.6	70	52.1	51.5	49.1
x00511a3	150	550	0.883	6.9	15	0.011	0.9	69.6	1.8	70	62.3	61.8	61.6
x00511a4	150	550	0.916	1.6	15	0.013	1.2	63.6	1.6	70	62.4	62.0	58.5
x00539a1	250	570	0.764	0.4	15	0.028	1.8	19.5	2	70	56.2	55.6	59.2
x00539a3	250	570	0.74	1.1	15	0.029	1.9	16.9	5.2	70	59.9	59.3	60.3
x00629b3	150	540	0.908	4.9	14	0.032	0.8	26.6	1.5	70	86.4	87.1	87.6
x00629b4	150	500	0.853	1.9	10	0.079	4.7	10.5	3.6	70	105.1	107.3	94.5
x00629c1	150	540	0.862	10.1	14	0.035	2.6	24	0.1	70	78.3	78.6	81.0
x00629d2	150	570	0.873	3.2	17	0.053	3.7	18	2.3	70	71.9	72.0	68.4
x00636a2	0	570	0.823	11	18	0.042	5.6	22	3.8	70	44.6		
x00665a1	0	350	0.939	2.4	7	0.037	0.4	12.6	2.5	30	70.2	72.0	60.7
x00665a2	150	350	0.766	9.8	5	0.033	2.6	15.4	0.6	30	66.4	68.0	67.2
x00665a3	150	350	0.888	2.4	5	0.013	0.7	39.8	2.5	30	75.6	77.9	74.3
x00665b2	150	570	0.824	3.5	17	0.021	1.5	38.5	1.9	70	74.7	74.9	75.7
x00666b1	150	520	0.868	7.2	12	0.04	3	17.4	6.1	70	92.2		81.9
x00666b2	150	520	0.91	13.5	12	0.023	2.1	32.1	0.3	70	100.2		99.2
x00666b3	150	350	0.73	6.4	5	0.073	1.1	6.6	1.7	70	95.1	95.1	91.3
x00666b4	150	530	0.806	0.8	13	0.034	3.4	22	1.3	70	72.4	72.6	68.2
x00670b2	0	350	0.829	16.9	6	0.064	5.6	9.8	9.6	70	129.7		114.7
x00670b8	0	425	0.973	1.3	8	0.092	0.8	7.4	6.1	70	144.7		
x00671b3	150	550	0.905	4.7	15	0.046	2.3	19.1	3.7	70	71.4	71.5	72.0
x00671b4	150	550	0.879	8.4	15	0.056	7.8	16.4	3.8	70	74.9	75.5	
x00674b2	200	560	0.837	4.8	15	0.039	4.2	21.4	1.6	70	77.7	77.8	68.3
x00674b3	200	560	0.799	4	15	0.044	5	19.4	2.7	70	76.5	76.5	71.0

(continued on next page)

Table 2 (*continued*)

Specimen	T_{min}	T_{max}	f_{vds}	DRATS (%)	N	β	DANG	q	γ	B_{lab} (μT)	B_{raw} (μT)	B_{nlt} (μT)	B_{ani} (μT)
x00674b4	150	550	0.834	10.1	15	0.051	3.6	16.7	3.5	70	95.5	96.5	86.5
x00707a3	200	510	0.735	1.2	10	0.064	6.9	11.3	3.2	70	74.8		
x00754a1	150	570	0.912	1.2	19	0.011	0.8	73.8	0.8	50	73.6		
x00754b1	0	580	0.968	1	21	0.02	1.3	43.5	1.4	50	70.8		
x00754c1	150	570	0.909	0.6	19	0.008	0.7	91.4	2.2	50	74.8		
x00754x1	150	580	0.926	1.3	20	0.012	0.7	66.8	1.1	50	74.6		
x00754x2	150	580	0.933	0.8	20	0.012	0.5	65	0.5	50	73.9		
x00754x3	150	580	0.943	4.9	20	0.014	0.6	55.7	3.1	50	72.2		
x00754x4	150	580	0.93	1.1	20	0.012	0.3	63.3	0.7	50	76.1		
x00754x5	150	580	0.936	2.5	20	0.012	0.5	64.3	1.4	50	76.7		
x00754x6	150	580	0.917	2	20	0.011	0.6	73.4	2	50	68.1		
x00754x7	150	580	0.916	0.9	20	0.008	1.3	96.8	4.1	50	68.2		
x00754x8	150	580	0.956	2	20	0.008	0.9	98	2.9	50	74.7		

For cut-off values see Table 1; T_{min} and T_{max} are the minimum and maximum temperature steps used in the calculation. f_{vds}, DRATs β, DANG, q and γ are as defined by Tauxe et al. (2009). N is the number of temperature steps included in the slope estimate; B_{raw} = intensity without corrections; B_{nlt} = intensity after correction for non-linear acquisition; B_{ani} = intensity after correction for anisotropy.

Sum (DRATS), β, f_{vds}, Maximum Angle of Deviation (MAD) and the Deviation ANGle (DANG) (see Ben-Yosef et al. 2008a and Tauxe , 2009 for detailed definitions of these parameters). All the specimens meeting these very strict criteria are listed in Table 2, together with the commonly used statistic q defined by Coe et al. (1978) and γ of Tauxe (2009) (see description above). Only samples with two or more 'successful' specimens and a standard deviation of less than 20% of the mean were included in our final collection of high quality archaeointensity dataset (see Table 3). All paleomagnetic data, including measurements, specimen intensity values and selection criteria will be archived in the MagIC database (earthref.org).

3. Chronological considerations

The location and context of samples with 'successful' specimens are shown in Fig. 4. The section diagrams were used to place our results in strict chronological order (Fig. 5). Although thirteen high precision AMS radiocarbon measurements accompany the archaeointensity results (Fig. 4, Table 2; see Levy et al., 2008) and nine more come from nearby contexts (Levy et al., 2008), the standard deviations of the ages do not allow direct linking between precise ages and intensities. This is true despite our efforts to obtain 'short-life' carbon samples (using the outer rim of charcoals and seed samples) for avoiding the 'old wood effect', and the fact that the radiocarbon calibration curve is relatively steep in the relevant time frame (Ramsey et al., 2006). To achieve a sub-century resolution and a chronologically ordered sequence in sections made of non-horizontal archaeological layers, we assigned each sample a composite stratigraphic height ('Height' in Table 3), representing its elevation above selected contacts (red lines in Fig. 4). The selected contacts are distinct and can be traced through the two major sections (the eastern and southern sections respectively); their height (marked on Fig. 4) represents the cumulative maximum thickness of the units below, hence it is not equal to their absolute elevation and, for example, two samples with the same absolute elevation above sea level may have different composite stratigraphic height representing their relative stratigraphic ordering (compare for example B.10265 and B.20002 in Fig. 4, southern section).

Table 3
A summary of archaeointensity results from Khirbat en-Nahas, Jordan (latitude 30.681, longitude 35.437, 10th–9th centuries BCE).

Sample	Basket/locus	Material	Height (Cm)	B (uT)	σ (%)	N	VADM (ZAm^2)
b09664a	B.9664	Pot sherd	4.5	62.8	4.5	5	121.4
e10462a	B.10462	Slag	2.05	57	4.3	3	110.2
e10474a	B.10474	Slag	1.75	80.3	9.7	2	155.3
e10482a	B.10482	Slag	6.8	67.2	4.5	5	130
s10265a	B.10265	Slag	3.2	110.2	10.1	5	213.1
s20001a	B.20001	Tuyère	3.5	75.2	2.3	2	145.4
s20002a	B.20002	Tuyère	3.4	60.8	10.5	9	117.6
s20007a	B.20007	Pot sherd	2.95	77.5	9.2	5	149.9
x00511a	L.511	Slag	7.1	58.5	11.6	4	113.1
x00539a	L.539	Slag	5.1	59.7	1.3	2	115.4
x00629b	L.629	Furnace fragments	3.8	91	5.4	2	176
x00665a	L.665	Slag	2.45	67.4	10.1	3	130.3
x00666b	L.666	Slag	1.65	85.1	15.7	4	164.6
x00670b	L.670	Furnace fragments	1.35	129.7	16.3	2	250.8
x00671b	L.671	Slag	1.2	73.4	2.8	2	141.9
x00674b	L.674	Slag	1	75.2	13.1	3	145.4
x00754x	L.754	Pot sherd	4.8	73.1	4.6	8	141.4

Height is in composite meters (see text); B = ancient field intensity value, VADM = Virtual Axial Dipole Moment values; σ is the standard deviation of the mean as a percentage of the mean, and N is the number of specimens included in the mean calculation.

The contact line at 3.2 composite meters (Cm) height (Fig. 4, and inset to Fig. 5) is a major stratigraphic boundary, separating archaeological strata M3 and M2 (Levy et al., 2008). This was inferred to be a major re-organization of the copper production enterprise and may represent a hiatus of several decades or more.

The maximum and minimum age constraints over the part of the excavation that yielded the archaeointensity data listed in Table 3 span approximately 200 yr, from 983 ± 25 to 816 ± 17 BCE (1 σ probabilities, Fig. 5). Although we do not presume a constant rate of accumulation, as the nature of anthropogenic debris is complex and include social and other non-predictable factors, ordering our samples according to their composite height is the best approximation at relative age and does allow sub-century resolution. Slag and other metallurgical debris represent the time of their immediate use (in contrast to archaeointensity of ceramic sherds that may have an inherent heirloom or usage time discrepancies) a quality that further supports the interpretation of composite height sequencing as chronological ordering. All of the samples came from a similar type of site formation process, except for two ceramic sherds that were collected from different floor levels of a nearby structure (L.635 and L.754 in the eastern section of Fig. 4); these are distinguished with different symbols (black diamonds) in Fig. 5, as their intensity measurements may be overestimated by up to 10% (assuming a cooling period of maximum 15 h, see e.g., Genevey et al., 2003) and some other inherent differences may be present (as the long 'use-life' of pots mentioned above). It is important to note that in this type of archaeological record, hiati of a few decades between nearby data points are likely, and that the deposition process is significantly different than in a geological setting.

Using the Bayesian statistics of the radiocarbon measurements, the general stratigraphic division of the excavation, and historical considerations (Levy et al., 2008), we can add a few additional chronological markers. According to the radiocarbon data analysis, the boundary

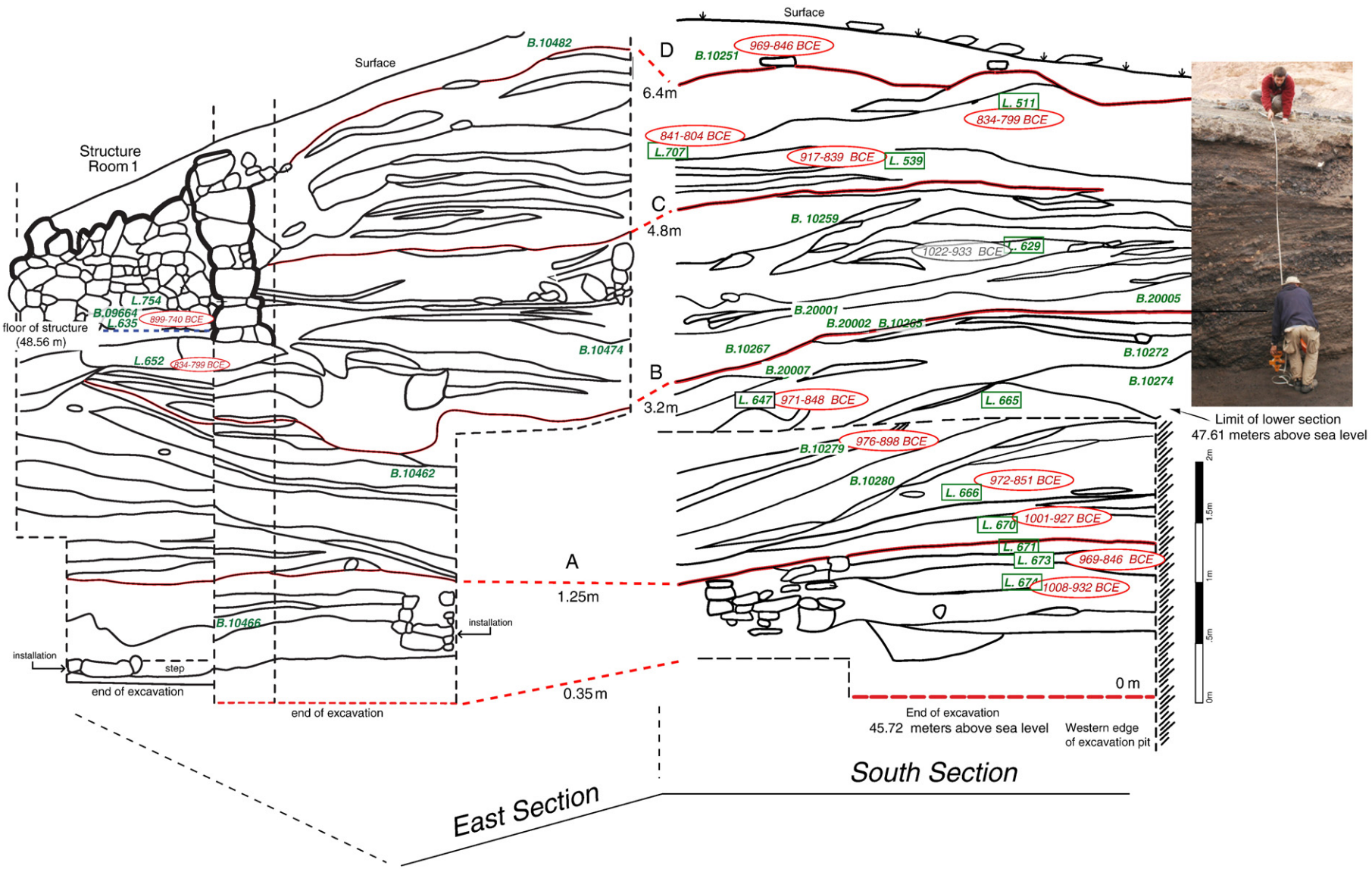

Fig. 4. Khirbat en-Nahas, area M (Faynan Copper Ore District, Jordan): drawing of the eastern (left) and southern (right) walls of excavation pit in a 'slag mound' depicting multi-layer sequence of copper production debris and location of all samples with 'successful' archaeointensity specimens obtained directly from these walls ('B' numbers for Baskets) or from the associated excavation ('L' numbers for Loci) (samples with specimen averages having $\sigma < 20\%$ of the mean are listed in Table 3). Results from radiocarbon samples are marked by circles (see Table 4; grey indicates an outlier). Also indicated as heavy lines are the reference stratigraphic horizons for composite stratigraphic height measurements (cf. Table 3 and text). (For interpretation of the references to color in this figure legend, the reader is referred to the web version of this article.)

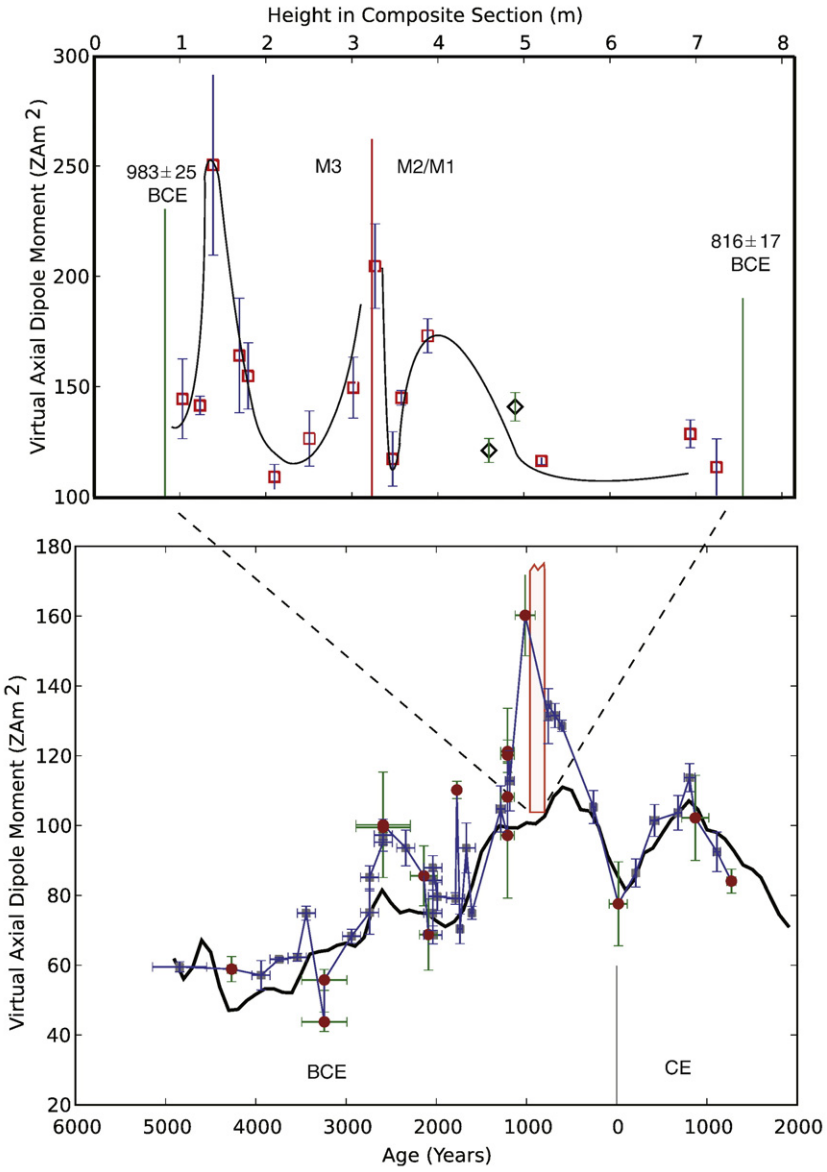

Fig. 5. Virtual axial dipole moments (VADMs) of the geomagnetic field for the last seven millennia and the spike recorded in this study (note that 'Z' stands for 10^{21}). Southern Levantine data are from Ben-Yosef et al. (2008a,b) (red circles), northern Levantine data are from Genevey et al. (2003) and Gallet et al. (2006) (grey squares), and the CALS7k.2 model is of Korte and Constable 2005) (black curve). Inset shows data from this study; a line is sketched through the data points as a visual aid, emphasizing trends and possible major hiatus. Note changes of scale, and the boundary line of Strata M3/M2 discussed in the text. (For interpretation of the references to color in this figure legend, the reader is referred to the web version of this article.)

Table 4
Radiocarbon dates.

OxA-#	Basket#	Locus#	Material	Species	Date BP	+/−	Cal. date BCE 68.2%
17630	10251	502/503	Charcoal	*Retama raetam*	2764	25	969–846
12436	8501	511	Charcoal	*Tamarix?*	2659	32	834–799
17639	10116	707	Charred seeds	*Phoenix doctylifera*	2678	26	841–804
12437	9039	539	Charcoal	*Tamarix?*	2746	35	917–839
17637	9244	629	Charcoal	*Phoenix doctylifera*	2836	26	1022–933
17641	9561	647	Charcoal	*Acacia* sp	2767	25	971–848
17642	10279	665	Charcoal	*Tamarix* sp	2781	25	976–898
17640	9835	666	Charcoal	*Tamarix* sp	2770	25	972–851
17643	9903	670	Charcoal	*Tamarix* sp	2813	26	1001–927
17647	9912	673	Charcoal	*Haloxylon persicum*	2764	25	969–846
17644	9927	674	Charcoal	*Tamarix* sp	2824	25	1008–932
17636	9228	635	Charred seeds	*Phoenix doctylifera*	2732	25	899–840
17645	9626	652	Charcoal	*Tamarix* sp	2747	25	913–843

After Levy et al. 2008; see Fig. 2 for context of samples.

between M3 and M2 is approximately the 10th/9th centuries BCE transition, with a high probability that the stratigraphic break represents the campaign of the Egyptian Pharaoh Sheshonq (Shishak) I in the region, dated to ca. 925 BCE (red line in inset to Fig. 5). The highest probability for the beginning of stratum M2 is after 910 BCE. The boundary between strata M1 and M2 is not well defined stratigraphically or by the radiocarbon results. Any other derivatives of the Bayesian modeling suggest even shorter time intervals for the archaeological accumulation of strata M1–3.

4. Results and discussion

A total of 91 specimens out of 340 measured passed our strict selection criteria (Table 2). The primary cause for failure was low f_{vds} values, as we insisted on single component magnetization for avoiding problematic interpretations. The anisotropy correction, when applied, was on average 5.5 ± 5.4% and not more than 25%; for a proxy to the anisotropy of a specimen, we have used the γ in Table 3 and made sure that the non-corrected specimens have low γ values. Exceptions to this were two specimens with γ values greater than 5° that broke prior to the AARM correction. The TRM non-linear acquisition corrections are much less significant and show changes of up to 13% with an average change of 2%. We considered as reliable results only samples with at least two successful specimens that demonstrate internal consistency (σ<20%). These are listed in Table 3. These have also been converted to virtual axial dipole moments (VADM; see description in e.g., Tauxe, 2009).

The recorded values of the geomagnetic field intensity range from 57 μT (VADM of 110 ZAm^2) to 130 μT (VADM of 251 ZAm^2) (Fig. 5, Table 3) and include values higher than all of the over 3500 intensity results (with the same standard deviation cut-off) documented for the last 50,000 yr (based on search of the geomagia.ucsd.edu website). Our highest VADM result has a standard deviation of 16%; this should be viewed as excellent reproducibility, because the non-linear correction becomes more extreme at high intensity values (see e.g., specimen s10265a3 in Fig. 2) (Selkin et al., 2007), thus reproducibility becomes more difficult to achieve.

Fig. 5 documents 200 yr of high resolution field behavior during a period of overall high intensity values. The geomagnetic feature starting near the bottom of the section with a high value of 251 ZAm^2 (L.670 at 1.35 m), dropping through a low of 109 ZAm^2 (B.10462 at 5.1 m) then rising again to 205 ZAm^2 (B.10265 at 3.2 m), constitutes a remarkable sequence of serially correlated intensity data sweeping out a change of more than a factor of two in field strength in what must have been a very short amount of time (at most 150 yr). For comparison, the present geomagnetic field evaluated with the International Geomagnetic Reference Field at Khirbat en-Nahas is 44 μT (VADM of 83 ZAm^2) and appears to be increasing at a rate of less than 4 μT per 100 yr.

Our results fit into a gap in the published dataset for the Levant (Genevey et al., 2003; Gallet et al., 2006; Gallet and Le Goff, 2006; Ben-Yosef et al., 2008a) (Fig. 5), and agree with the general tendencies of the previously published data. However, when widening the scope of comparison some discrepancies appear. Fig. 6 shows all of the paleo- and archaeointensity data from with 1000 mi of Jordan (locations shown in the inset) that have been uploaded into the Geomagia50 (geomagia.ucsd.edu) database (Korhonen et al., 2008) having at least 2 specimens and a sample average with a standard deviation less than 15%. Highlighted as blue squares are the Levantine data from Ben-Yosef et al. (2008a,b), Genevey et al. (2003) and Gallet et al. (2006) (see also Fig. 5). Three realizations, of the CALS7K.2 model of Korte and Constable (2005) evaluated at the locations of the stars in the inset, are plotted as thin lines. Also shown (black diamonds) is the Grecian master curve of De Marco et al. (2008). For reference, we plot bounds on the equivalent

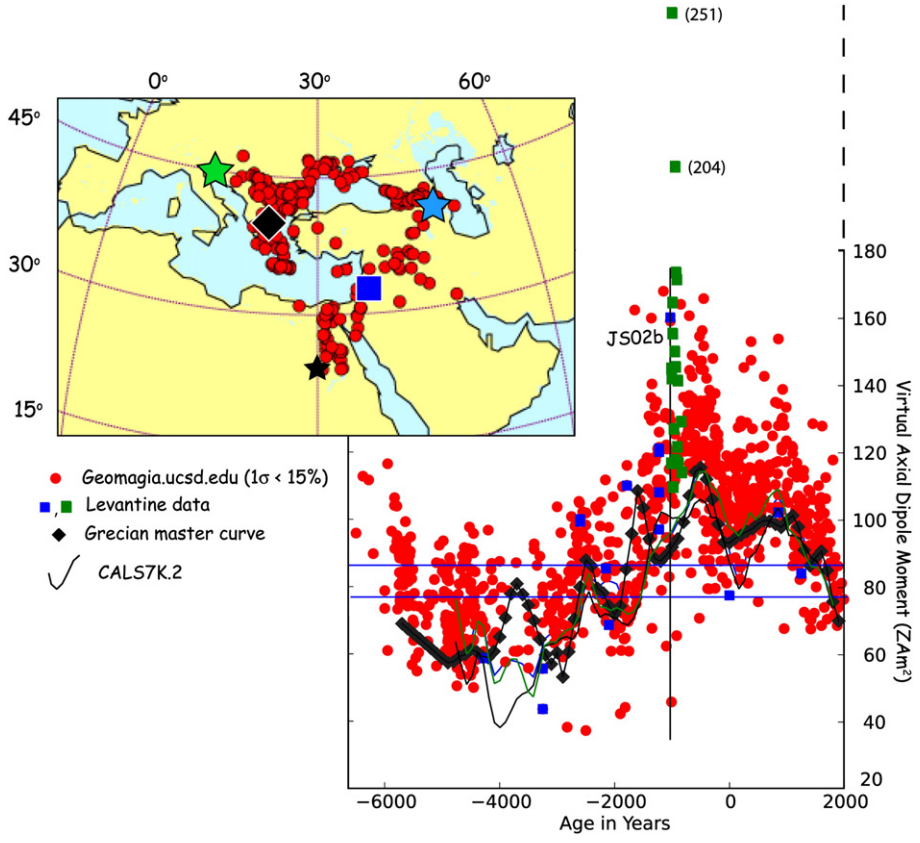

Fig. 6. Selected data from within 1000 mi of Jordan (locations in inset) with N>1 specimens and σ<15% from geomagia.ucsd.edu. Grecian master curve: model of De Marco et al. (2008). CALSK7.2: 3 realizations from locations shown in inset. Bounds on the VADMs of the preset field values at the observation sites in the inset are shown as horizontal blue lines (77–87 ZAm^2). (For interpretation of the references to color in this figure legend, the reader is referred to the web version of this article.)

values of the present (2005) field estimated from the international geomagnetic reference field (IGRF) at the observation sites shown in the inset. Although there are recognizable broad trends in the data, there is a considerable scatter. The high field values of this study and the one published for Khirbat al-Jariya (JS02b) (Ben-Yosef et al., 2008a) correspond to a time of rather low intensity in, for example, the Grecian master curve. The cause of the discrepancy and scatter in the data could be 1) genuine geomagnetic field behavior in which there can be factor of two differences in intensity on short spatial scales, 2) uncertainties in dates of samples in times of high geomagnetic field variability, and 3) unreliable intensity estimates. Variability in the present field at these observation sites (shown by the horizontal blue lines in Fig. 5) is a little more than 10%. Experimental results from our synthetic slags suggest a potential uncertainty of the method of another roughly 10%. Factor of two differences are difficult to ascribe to inherent geomagnetic field variability on short spatial scales or to data unreliability. Further research is needed to enhance our understanding of the regionality of unique features of the geomagnetic field behavior.

Rapid changes in archaeointensity have been noted in previous studies (Gallet and Le Goff, 2006; Ben-Yosef et al., 2008a; Genevey et al., 2009), but not within a tight stratigraphic context and not reaching the peak intensities recovered here. High field values for the same period were obtained from the Western USA (Champion, 1980; Hagstrum and Champion, 2002) (values up to 140 ZAm^2), and even higher values of almost 200 ZAm^2 from Hawaii (Pressling et al., 2006). These data suggest the possibility of a global spike, and encourage further investigation of the regional extent of this feature. However, the samples from Hawaii were re-measured using the microwave technique and yielded lower results (Pressling et al., 2007), and the chronological constraints over the rate of changes observed in these studies are still relatively poor. Also, the disagreement between the Levantine and Grecian curves during this time interval underscore the difficulty of directly comparing results with variable chronological constraints.

Archaeo- and paleomagnetic data are often used for comparison with numerical models of geomagnetic field behavior (e.g., Kono and Roberts, 2002). Some of the numerical models apparently can produce large, local field anomalies during, for example, equatorial magnetic upwellings (Aubert et al., 2007), but such features hitherto have not been observed in models constructed from human measurements of the geomagnetic field (e.g., the GUFM model of Jackson et al., 2000) or in models constructed from archaeo- and paleomagnetic data (e.g., CALS7.2 k of Korte and Constable, 2005). Models of geomagnetic secular variation are only as good as the data that constrain them and large age uncertainties combined with data of variable quality will tend to smooth out model predictions. The existence of very large, perhaps local, field spikes makes the construction of paleosecular variation models more complex; however, the possibility of their occurrences and the spike documented in this study should be taken into consideration when calculating numerical models or compiling regional datasets.

Sequences of high resolution archaeointensity results may serve as an additional dating reference for archaeological sites. The 200 yr covered by our study (the 10th and 9th centuries BCE) represent a contentious period in the historical biblical archaeology of the region (e.g., Levy and Higham, 2005). We suggest that the geomagnetic intensity imprint on the archaeological record recovered here can be used as an additional reference for dating key sites of this formative period in the history of the Southern Levant (the development of local and influential polities such as Israel, Edom and Moab and the debated 'Solomonic Kingdom').

The geomagnetic features documented in this study shows that over short intervals of time the field can reach very high intensities. Because of the short duration such features are easily missed in common archaeo and paleo magnetic investigation and the reported peak is currently unique, with its geographic extent still unknown. Our results illustrate the efficacy of combining high precision in archaeological recording, high resolution of radiocarbon dating and systematic archaeointensity experiments for tracing and studying such unusual features of the geomagnetic field. Although elusive, relevant fields of research should take into account such features when modeling the geomagnetic field and geomagnetic-related phenomena.

Acknowledgments

We thank Jason Steindorf for many of the measurements, Amotz Agnon and Jeff Gee for their comments and Dr. Fawwaz al-Khraysheh, Director General, Department of Antiquities of Jordan for his support of the archaeological field work. Paleomagnetic and rock magnetic measurements were done primarily at the paleomagnetic laboratories of SIO with ATRM and TRM acquisition studies being done at HUJI. This study was supported by the US–Israel Binational Science Foundation Grant No. 2004/98, NSF grant EAR0636051 and the US–Israel Educational Foundation Fulbright Grant for Ph.D. students 2006–2007.

We also thank Carlo Laj and an anonymous reviewer for their insightful comments that helped to improve the text of this paper.

References

Aubert, J., Aurnou, J., Wicht, J., 2007. The magnetic structure of convection-driven numerical dynamos. Geophys. J. Int. 172, 945–956.
Ben-Yosef, E., Ron, H., Tauxe, L., Agnon, A., Genevey, A., Levy, T.E., Avner, A., Najjar, M., 2008b. Application of copper slag in geomagnetic archaeointensity research. J. Geophys. Res. 113, B08101.
Ben-Yosef, E., Tauxe, L., Ron, H., Agnon, A., Avner, A., Najjar, M., Levy, T.E., 2008a. A new approach for geomagnetic archaeointensity research: insights on ancient metallurgy in the Southern Levant. J. Archaeol. Sci. 35, 2863–2879.
Champion, D.E., 1980. Holocene geomagnetic secular variation in the Western United States: implications for the global geomagnetic field. Rept.Open File Series U.S. Geol.Surv. 80-824, pp. 314–354.
Christensen, U.R., Wicht, J., 2007. Numerical dynamo simulations. Treatise Geophys. 8, 245–282.
Coe, R.S., Gromme, S., Manknen, E.A., 1978. Geomagnetic paleointensities from radiocarbon-dated lava flows on Hawaii and the question of the Pacific nondipole low. J. Geophys. Res. 83, 1740–1756.
De Marco, E., Spatharas, V., Gomez-Paccard, M., Chauvin, A., Kondopoulou, D., 2008. New archaeointensity results from archaeological sites and variation of the geomagnetic field intensity for the last 7 millennia in Greece. Phys. Chem. Earth 33 (6–7), 578–595.
Gallet, Y., Le Goff, M., 2006. High-temperature archeointensity measurements from Mesopotamia. Earth Planet. Sci. Lett. 241, 159–173.
Gallet, Y., Genevey, A., Le Goff, M., Fluteau, F., Eshraghi, S.A., 2006. Possible impact of the Earth's magnetic field on the history of ancient civilizations. Earth Planet. Sci. Lett. 246, 17–26.
Genevey, A., Gallet, Y., Margueron, J., 2003. Eight thousand years of geomagnetic field intensity variations in the eastern Mediterranean. J. Geophys. Res. 108. doi:10.1029/2001JB001612.
Genevey, A., Gallet, Y., Rosen, J., LeGoff, M., 2009. Evidence for rapid geomagnetic field intensity variations in Western Europe over the past 800 years from new French archaeointensity data. Earth and Plan. Sci. Lett 284, 132–143.
Glatzmaier, G.A., Roberts, P.H., 1996. Rotation and magnetism of Earth's inner core. Science 274, 1887–1891.
Hagstrum, J.T., Champion, D.E., 2002. A Holocence geomagnetic secular variation record from 14C-dated volcanic rocks in Western America. J. Geophs. Res. 107 (B1), 2025. doi:10.1029/102001/JB000524.
Jackson, A., 2003. Intense equatorial flux spots on the surface of the Earth's core. Nature 424 (6950), 760–763.
Jackson, A., Jonkers, A.R.T., Walker, M.R., 2000. Four centuries of geomagnetic secular variation from historical records. Philos. Trans. R. Soc. Lond. Ser. A 358 (1768), 957–990.
Kono, M., Roberts, P.H., 2002. recent geodynamo simulations and observations of the geomagnetic field. Rev. Geophys. 40. doi:10.1029/2000RG000102.
Korhonen, K., Donadini, F., Riisager, P., Pesonen, L.J., 2008. GEOMAGIA50: an archeointensity database with PHP and MySQL. Geochem. Geophys. Geosyst. 9. doi:10.1029/2007GC1001.
Korte, M., Constable, C., 2005. Continuous geomagnetic field models for the past 7 millennia: 2. CALS7K. Geochem. Geophys. Geosyst 6, Q02H16. doi:10.1029/2004GC000801.
Lanos, P., 2003b. Bayesian inference of calibration curve, application to archaeomagnetism. In: Buck, C.E., Millard, A.R. (Eds.), Tools for Chronology, Crossing Disciplinary Boundaries. Springer-Verlag, London, pp. 43–82.
Levy, T.E., Higham, T. (Eds.), 2005. The Bible and Radiocarbon Dating — Archaeology, Text and Science. Equinox, London.
Levy, T.E., Higham, T., Ramsey, C.B., Smith, N.G., Ben-Yosef, E., Robinson, M., Munger, S., Knabb, K., Schulze, J.P., Najjar, M., Tauxe, L., 2008. High-precision radiocarbon dating and historical biblical archaeology in Southern Jordan. Proc. Natl. Acad. Sci. 105, 16460–16465.

Opdyke, N.D., Channell, J.E.T., 1996. Magnetic Stratigraphy. Academic Press.
Pressling, N., Laj, C., Kissel, C., Champion, D., Gubbins, D., 2006. Paleomagnetic intensity from 14C-dated lava flows on the big Island, Hawaii: 0–12 kyr. Earth Planet. Sci. Lett. 247, 26–40. doi:10.1016/j.epdl.2006.1004.1026.
Pressling, N., Brown, M.C., Gratton, M.N., Shaw, J., Gubbins, D., 2007. Microwave paleointensities from Holocene age Hawaiian lavas: Investigation of magnetic properties and comparison with thermal paleointensities. Phys. Earth Planet. Inter. 162, 99–118. doi:10.1016/j.pepi.2007.1003.1007.
Ramsey, C.B., Buck, C.E., Manning, S.W., Reimer, P., van der Plicht, H., 2006. Developments in radiocarbon calibration for archaeology. Antiquity 80, 783–798.
Selkin, P., Gee, J., Tauxe, L., 2007. Nonlinear thermoremanence acquisition and implications for paleointensity data. Earth Planet. Sci. Lett. 256 (1–2), 81–89.
Tarduno, J.A., Cottrell, R.D., Smirnov, A.V., 2006. The paleomagnetism of single silicate crystals: recording geomagnetic field strength during mixed polarity intervals, superchrons, and inner core growth. Rev. Geohys. 44, RG1002. doi:10.1029/2005RG000189.
Tauxe, L., 2009. Essentials of Paleomagnetism, University of California Press, Berkeley.
Tauxe, L., Staudigel, H., 2004. Strength of the geomagnetic field in the Cretaceous Normal Superchron: new data from submarine basaltic glass of the Troodos Ophiolite. Geochem. Geophys. Geosyst. 5 (2), Q02H06. doi:10.1029/2003GC000635.
Torsvik, T.H., Mueller, R.D., van der Voo, R., Steinberg, B., Gaina, C., 2008. Global plate montion frames: toward a unified model. Rev. Geophys. 46, RG3004.